SCIENCE CHINA
Information Sciences

• RESEARCH PAPER •

October 2022, Vol. 65 202201:1–202201:18
https://doi.org/10.1007/s11432-020-3255-5

Multi-objective optimization for 10-kW rated power dynamic wireless charging systems of electric vehicles

Ze ZHOU[1], Zhitao LIU[1*], Hongye SU[1] & Liyan ZHANG[2]

[1]*State Key Laboratory of Industrial Control Technology, Institute of Cyber-Systems and Control, Zhejiang University, Hangzhou* 310027*, China;*
[2]*School of Automation, Wuhan University of Technology, Wuhan* 430070*, China*

Received 23 September 2020/Revised 17 January 2021/Accepted 1 April 2021/Published online 23 September 2022

Abstract In this paper, we propose a method to optimize the output power, efficiency, and cost of the dynamic wireless charging (DWC) system of electric vehicles by using the transmitting coil spacing as the decision variable. In a set of transmitting equipment, we adopt a structure with two transmitting networks in parallel and derive loss models. The expressions of the output power and efficiency of the DWC system are obtained by data fitting. In addition, combined with the proposed cost function, we construct a multi-objective optimization problem on output power, efficiency, and cost. Due to the complexity of the objective function, it is difficult to solve the problem by the analytic method, and thus we propose a constrained adaptive particle swarm optimization (CAPSO) algorithm with high accuracy to solve the problem. Finally, the simulation results verify the feasibility of the proposed model. The advantages of the proposed CAPSO algorithm and the optimization results under different weight combinations are presented.

Keywords dynamic wireless charging, electric vehicles, multi-objective optimization, constrained adaptive particle swarm optimization

Citation Zhou Z, Liu Z T, Su H Y, et al. Multi-objective optimization for 10-kW rated power dynamic wireless charging systems of electric vehicles. Sci China Inf Sci, 2022, 65(10): 202201, https://doi.org/10.1007/s11432-020-3255-5

1 Introduction

As a method to replace traditional plug-in charging, electric vehicle (EV) wireless charging technology has the advantages of simple operation, safety, and reliability. Nowadays, a large number of researchers have investigated the field of wireless charging, including magnetic coupling coils, compensation structures, and control methods. Magnetic coupling coils are mainly circular pads, double-D (DD) pads, bipolar pads, and DD quadrature pads [1–3]. These factors need to be considered in the design of magnetic coupling coils, such as small size, low cost, high coupling coefficient, high offset margin, high transmission distance, good shielding effect, and high biosafety. According to the series-parallel forms of capacitors at the transmitting and receiving sides, fundamental compensation structures can be divided into series-series, series-parallel, parallel-series, and parallel-parallel [4]. Based on these fundamental structures, researchers combine capacitors and inductors to derive a series of compensation structures, such as LCC-CCL [5–7]. Here, L denotes an inductor and C denotes a capacitor. LCC-CCL denotes a symmetrical resonance network. Compared with other structures, the LCC-CCL structure is able to make the resonance frequency independent of the coupling coefficient and load, achieve constant current output, and improve the power factor, thereby reducing control difficulty and improving energy transmission efficiency [8]. Moreover, the LCC-CCL structure can filter out the harmonics introduced by the inverter and rectifier, thus improving power quality. Accordingly, this paper adopts the LCC-CCL structure. Control methods are mainly used to improve the dynamic and stable performance of wireless charging systems. According to the positions where the control strategies are applied, they are divided into transmitting side control [9, 10], receiving side control [11, 12], and bilateral control [13]. Indeed, these researches ensure the rapid development of

* Corresponding author (email: ztliu@zju.edu.cn)

wireless charging technology. However, the static wireless charging cannot solve the problems of the short range and large battery pack of EVs as well as range anxiety. Therefore, researchers begin to consider dynamic wireless charging (DWC) as a solution to the above problems.

Many researchers have made contributions to the implementation of the DWC technology. The Oak Ridge National Laboratory introduces experience and challenges in EV-DWC research, and shows several experimental prototypes [14]. The Korean Advanced Institute of Science and Technology (KAIST) designs an EV-DWC system named the on-line electric vehicle [15]. Then, the KAIST studies the reliability of the EV-DWC system in the actual traffic environment. In addition, Utah State University establishes a 25-kW EV-DWC system [16]. Due to the offset of the energy receiving coil and the transmitting coil, researchers at the Utah State University regulate the system power by the phase shift control of the inverter at the transmitting side. Under DWC conditions, the movement of the EV will cause changes in the mutual inductance between the energy transmission coils, which will bring about power fluctuations. To stabilize the output power, Li et al. [17] utilized two transmitting coils with a T-type compensation structure to work at the same time. In addition, Vu et al. [18] proposed a multi-phase transmitter system to achieve low output power pulsation of the DWC system. In addition to focusing on DWC technology, there is also research on the combination of DWC technology and other technologies. For instance, under the background of EV-DWC, the research on the coordinated operation of power grid and transportation networks has become a hot issue [19–21]. The development of the DWC technology is able to accelerate the promotion of EVs because it has the advantages of increasing the endurance mileage of EVs, easing range anxiety, and reducing the size and cost of the onboard battery pack. Meanwhile, the DWC technology can strengthen the connection between EVs and the power grid, forming the integration of EVs, power grid, and transportation, which can lay the foundation for the construction of smart transportation and smart city. Therefore, the DWC technology is the key to realizing multi-field technology integration.

The output power and efficiency of the DWC system are concerned indexes. The increased power can ensure the large electric energy supply of EVs within the unit time, so the power research of DWC systems is particularly important. Compared with the traditional single excitation unit, the double excitation unit is proposed to improve the system power [22]. Moreover, because the reduction of the coupling coefficient will lead to the power reduction in the dynamic process, Zhou et al. [8] proposed to add a direct current-direct current (dc-dc) converter at the energy receiving side of the DWC system to improve power compared to the state without dc-dc converter and employ model predictive control to the DWC system, which can effectively improve the system reliability. Based on the frequency division characteristics of the magnetic resonant wireless charging system, Zhao et al. [23] used a control algorithm to maintain constant power. Besides power, the efficiency of DWC systems is also a hot research issue. By improving the energy receiving coil, the EV can be stably charged under a certain transmission distance, and the transmission efficiency can be improved by 50% [24]. Moreover, using overlapped DD type coils to create a strong magnetic field can increase the DWC system efficiency [25]. Kim et al. [26] established the efficiency model of the multiple-transmitter DWC system, and optimized the current ratios of transmitting coils and the load on the receiving side to obtain the maximum efficiency.

In addition to the output power and efficiency, the cost of the DWC system is also a key index. The existing studies mainly focus on the optimization of output power or efficiency of the DWC system, and seldom take the output power, efficiency, and cost of the DWC system into comprehensive consideration. For the cost issue, we first need to determine the energy transmitting terminal structure of the DWC system. Indeed, DWC systems can be divided into long-track type [27,28] and short-individual type [29–31]. The advantage of long-track type DWC systems is simple structure, but its limitation is low efficiency. As presented in Figure 1, the structure of short-individual type DWC systems is very similar to the static wireless charging systems, except that there are multiple sets of independent transmitting equipment at the transmitting terminal. In addition, we define the circuit composed of the transmitting coil and its resonance network as the transmitting network. A set of transmitting equipment includes a high-frequency inverter and multiple transmitting networks in parallel. Each set of transmitting equipment can work independently, which can be switched and controlled by intelligent algorithms, thus greatly improving the energy utilization rate. Therefore, the short-individual type is an effective DWC form. The transmitting coil spacing of the short-individual type will affect the mutual inductance between the transmitting coils and the receiving coil, thus affecting the output power and efficiency of the DWC system. Meanwhile, the transmitting coil spacing also affects the DWC system cost because the spacing affects the number of laid transmitting equipment when the length of the charging track is constant. Therefore, the transmitting coil spacing is the key parameter of the DWC system. Then, we consider the

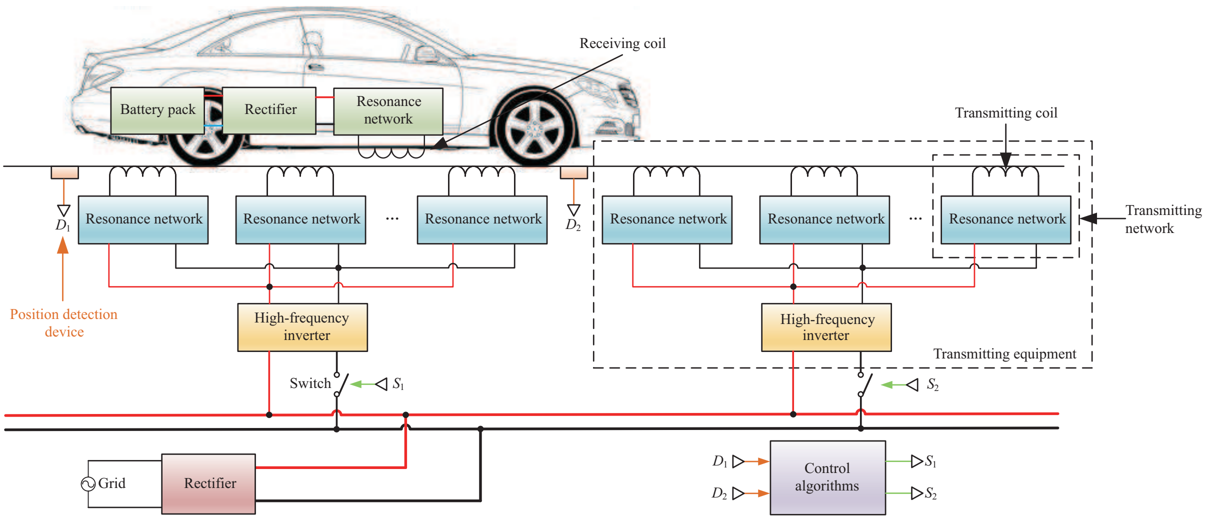

Figure 1 (Color online) Schematic diagram of short-individual type DWC systems.

comprehensive optimization of the output power, efficiency, and cost of the DWC system through the transmitting coil spacing, which is helpful to the advancement and implementation of the short-individual type DWC technology.

The main contributions of this paper are summarized as follows. First, we propose a multi-objective optimization for the output power, efficiency, and cost of the DWC system by taking the transmitting coil spacing as the decision variable. Second, based on the analysis in [5], we derive the loss models of the wireless charging system in detail, including the high-frequency inverter loss model, the LCC-CCL resonance network loss model, and the rectifier loss model. Third, according to [30], we give the current expressions of the LCC-CCL resonance network when multiple transmitting networks are in parallel. Moreover, we establish a model of multiple transmitting coils and a single receiving coil in ANSYS. The simulation results show that two transmitting networks in parallel have a good effect. Correspondingly, we adopt a structure in which two transmitting networks are in parallel. Fourth, we propose the constrained adaptive particle swarm optimization (CAPSO) algorithm for solving the multi-objective optimization problem. Compared with the conventional constrained particle swarm optimization (CPSO) algorithm, the CAPSO adaptively changes the inertia weight, self-learning factor, and swarm learning factor, thus having higher accuracy. Fifth, the simulation results demonstrate the rationality and effectiveness of the proposed model, and the superiority of the proposed CAPSO algorithm. In addition, the results of multi-objective optimization under different weight combinations are displayed.

The remainder of this paper is organized as follows. Section 2 presents the analysis of loss models. Section 3 illustrates the analysis of multiple transmitting networks. Moreover, the multi-objective optimization strategy is presented in Section 4. The simulation results are shown in Section 5. The conclusion is given in Section 6.

2 Loss models

Figure 2 presents a wireless charging system topology with internal impedance and the meanings of the symbols in Figure 2 are shown in Table 1. To clearly present the loss model, we first use the static wireless charging topology in Figure 2 to derive the loss model. When the mutual inductance M in Figure 2 changes, this topology can be regarded as a DWC system. In Subsection 3.1, we will extend the static charging topology to the DWC topology. Further, in Subsection 4.1, we will derive the loss model of the DWC system and construct the multi-objective optimization problem.

According to the analysis in [5], we can obtain the current expressions in the LCC-CCL resonance

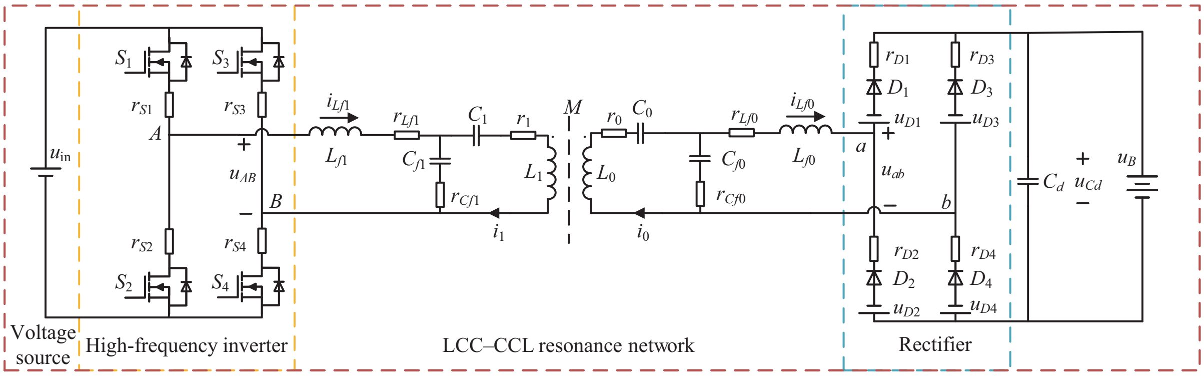

Figure 2 (Color online) Topology of the wireless charging system.

Table 1 Meanings of the symbols

Symbol	Parameter	Symbol	Parameter
S_x	MOSFET x	r_{Sx}	Internal resistance of S_x
L_{f1}	Primary-side resonance inductor	C_{f1}	Primary-side resonance capacitor
C_1	Primary-side compensation capacitor	L_1	Primary-side transmitting coil
L_{f0}	Secondary-side resonance inductor	C_{f0}	Secondary-side resonance capacitor
C_0	Secondary-side compensation capacitor	L_0	Secondary-side receiving coil
r_{Lfx}	Internal resistance of L_{fx}	r_{Cfx}	Internal resistance of C_{fx}
r_x	Sum of the internal resistance of C_x and L_x	M	Mutual inductance between L_1 and L_0
D_x	Diode x	u_{Dx}	Threshold voltage of D_x
r_{Dx}	On-resistance of D_x	C_{d}	Filter capacitor
u_B	Battery	u_{in}	Inverter input voltage
u_{AB}	Inverter output voltage	i_{Lfx}	Current flowing through the inductor L_{fx}
i_x	Current flowing through the coil L_x	u_{ab}	Rectifier input voltage

network as follows:

$$\begin{cases} |I_{Lf1}| = \dfrac{M|U_{ab}|}{\omega L_{f1} L_{f0}}, \\ |I_1| = \dfrac{|U_{AB}|}{\omega L_{f1}}, \\ |I_0| = \dfrac{|U_{ab}|}{\omega L_{f0}}, \\ |I_{Lf0}| = \dfrac{M|U_{AB}|}{\omega L_{f1} L_{f0}}, \end{cases} \tag{1}$$

where the symbols denoted by $|I|$ and $|U|$ are the root mean square (rms) values of the fundamental waves of the current and voltage. It is worth noting that Eq. (1) is derived based on the ideal model without internal impedance. To simplify the calculation, we use (1) to approximate expressions of the wireless charging system with internal impedance.

2.1 Loss model of the high-frequency inverter

The loss of the metal-oxide-semiconductor field-effect transistor (MOSFET) comes from its conduction loss and switching loss. Adjusting the impedance of the resonant network can make the system impedance appear inductive, thereby ensuring the realization of zero voltage switching, so the switching loss reduces to a small value. Indeed, a MOSFET can be turned on without a threshold voltage and we only need to consider its on-resistance. The high-frequency inverter is composed of four MOSFETs of the same type, so the internal resistance is the same, i.e., $r_{S1} = r_{S2} = r_{S3} = r_{S4}$. Then, we have the conduction loss of the high-frequency inverter as follows:

$$P_{\mathrm{ic}} = 2|I_{Lf1}|^2 r_{S1} = \frac{2 r_{S1} M^2 |U_{ab}|^2}{\omega^2 L_{f1}^2 L_{f0}^2}. \tag{2}$$

When the MOSFET turns off, its parasitic capacitance can keep the voltage of the MOSFET close to zero. Therefore, the switching loss is very small in the turn-off process [32]. However, the zero voltage turn-on process of MOSFET is more complicated than zero voltage turn-off. Before the MOSFET turns on, the voltage of the parasitic capacitance needs to be released, and then the body diode of MOSFET is on. Since the turn-on voltage of the diode is almost zero, zero voltage turn-on can be achieved. According to the analysis of [5], the condition for achieving zero voltage turn-on is to keep the output current $i_{\rm off}$ of the inverter positive when another MOSFET in the same arm turns off. In other words, the output current of the inverter lags the output voltage of the inverter. Therefore, in the case of zero-voltage soft switching, the switching loss is the loss on the body diode. The expression of $i_{\rm off}$ is described as [5]

$$i_{\rm off} = \frac{\sqrt{2}|U_{ab}|^2}{\omega |U_{AB}| L_{f0}} \left(\frac{\Delta L_{e0}}{L_{f0}} - \frac{1}{4} \right) + \frac{\sqrt{2}|U_{AB}|}{4\omega L_{f1}} \tag{3}$$

with

$$\Delta L_{e0} = \frac{1}{\omega^2 C_0} - \frac{1}{\omega^2 (C_0 + \Delta C_0)},$$

where ΔC_0 is the adjustment value to ensure zero voltage soft-switching. Indeed, we can define the ratio of switching loss to conduction loss as follows:

$$r_{\rm p} = \frac{E_{\rm s}}{E_{\rm c}} = \frac{2 i_{\rm off} u_{\rm bd} t_{\rm d}}{P_{\rm ic} T_{\rm p}}, \tag{4}$$

where $E_{\rm s}$ and $E_{\rm c}$ represent the switching loss and conduction loss, respectively; $T_{\rm p}$ is the switching period of the inverter; $u_{\rm bd}$ is the forward voltage of the body diode; $t_{\rm d}$ is the dead time. Accordingly, the inverter loss is

$$P_{\rm hfi} = (1 + r_{\rm p}) P_{\rm ic}. \tag{5}$$

2.2 Loss model of the LCC-CCL resonance network

The components of the LCC-CCL resonant network are inductors and capacitors. First, we analyze the loss model of inductors. Obviously, the current in the LCC-CCL resonant network is high-frequency alternating current (ac), so the skin effect and proximity effect need to be analyzed.

2.2.1 *Skin effect*

When high-frequency currents pass through a conductor, the phenomenon that currents tend to the surface of the conductor is called the skin effect. The loss caused by skin effect is $P_{\rm s} = k_{\rm se} R_{\rm dc} I_{\rm se}^2$ where $k_{\rm se}$ denotes a skin-effect coefficient; $R_{\rm dc}$ is the dc resistance, and $I_{\rm se}$ is the current rms in the conductor [33]. In addition, the skin depth $\delta_{\rm d}$ represents the corresponding depth when the current density decreases to $\frac{1}{e}$ of the surface, and its expression is $\delta_{\rm d} = \sqrt{\frac{2}{\omega\gamma\mu}}$ where ω is the angular frequency, γ is the conductivity, and μ is the permeability. Indeed, the skin effect is negligible when the conductor radius is much less than $\delta_{\rm d}$. Figure 3 presents the simulation results of skin effect where ω is $2 \times \pi \times 85000$ rad/s, γ is 58×10^6 S/m, μ is $4\pi \times 10^{-7}$ H/m, and the average current density is 5 A/mm^2. Moreover, the skin depth $\delta_{\rm d}$ is 0.23 mm according to the above parameters. It can be concluded that when the conductor radius is less than its skin depth, the current density and ohmic loss are evenly distributed; when the conductor radius is greater than the skin depth, the current density is larger and larger from the inside to the outside, and the ohmic loss is unevenly distributed. Moreover, the numerical results of skin effect are shown in Table 2. Indeed, from the results in Figure 3 and Table 2, it can be seen that the influence of skin effect can be greatly reduced by litz wire composed of multi-strand enameled wires with a diameter of 0.1 mm.

2.2.2 *Proximity effect*

When high-frequency currents are flowing in opposite directions between two conductors, the phenomenon that currents will concentrate on the adjacent side of conductors is the proximity effect. According to [7], the ac resistance caused by proximity effect is $R_{\rm ac} = k_{\rm pe} R_{\rm dc}$ where $k_{\rm pe}$ denotes a proximity-effect coefficient and belongs to [1.5, 2.5]. We set the distance between the two wires as 0.01 and 0.1 mm, respectively, and the current frequency is 85 kHz. Then, the results are presented in Figure 4. When the

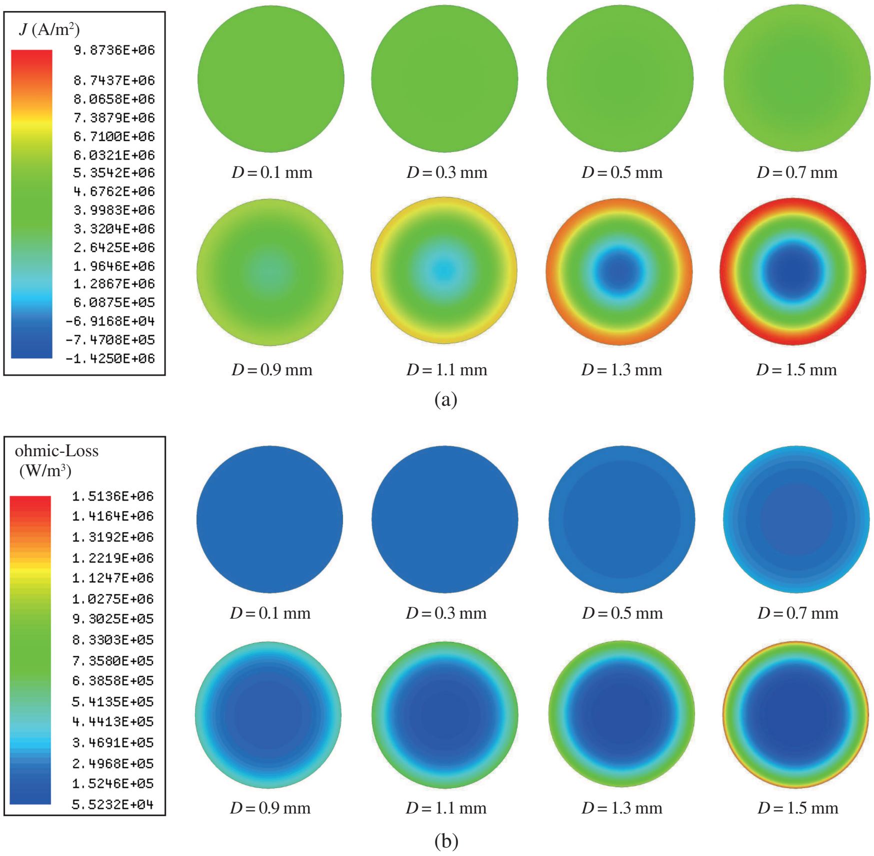

Figure 3 (Color online) Skin effect simulation results. (a) Current density distribution; (b) ohmic loss distribution.

Table 2 Numerical results of skin effect

Diameter (mm)	$\rho_{I\max}$ (A/m^2)	$\rho_{I\min}$ (A/m^2)	Ls$_{\max}$ (W/m^3)	Ls$_{\min}$ (W/m^3)
0.1	5.13E+06	5.13E+06	2.27E+05	2.27E+05
0.3	5.15E+06	5.09E+06	2.32E+05	2.26E+05
0.5	5.28E+06	4.84E+06	2.62E+05	2.20E+05
0.7	5.68E+06	4.08E+06	3.55E+05	2.03E+05
0.9	6.46E+06	2.71E+06	5.38E+05	1.72E+05
1.1	7.50E+06	9.84E+05	8.07E+05	1.30E+05
1.3	8.70E+06	3.25E+04	1.14E+06	8.81E+04
1.5	9.87E+06	6.92E+04	1.51E+06	5.52E+04

current directions are the same, the current is concentrated at the far end; when the current directions are opposite, the current is concentrated between the two wires. Therefore, the proximity effect will also cause the uneven distribution of high-frequency current and increase the loss.

According to the aforementioned analysis, the loss of skin effect can be minimized by using the litz wire composed of multi-strand wires with a diameter of 0.1 mm. Then, we only consider the ac loss caused by the proximity effect and dc loss.

The capacitor loss in the LCC-CCL network mainly comes from its parasitic resistance, and its expression is $r_C = \frac{D_F}{2\pi f C}$ where D_F, f, and C are the dissipation factor, frequency, and capacitance, respectively. The rms value of the current flowing through C_{f1} is $\sqrt{|I_{Lf1}|^2 + |I_1|^2}$ because the phase difference between the first-order signals of i_{Lf1} and i_1 is $\frac{\pi}{2}$, and C_{f0} is the same case [5]. Accordingly, we can obtain that the loss of the LCC-CCL resonant network is

$$P_{\mathrm{LCC}} = |I_{Lf1}|^2 r_{Lf1} + |I_{Lf0}|^2 r_{Lf0} + |I_1|^2 r_1 + |I_0|^2 r_0 + (|I_{Lf1}|^2 + |I_1|^2) r_{Cf1} + (|I_{Lf0}|^2 + |I_0|^2) r_{Cf0}. \quad (6)$$

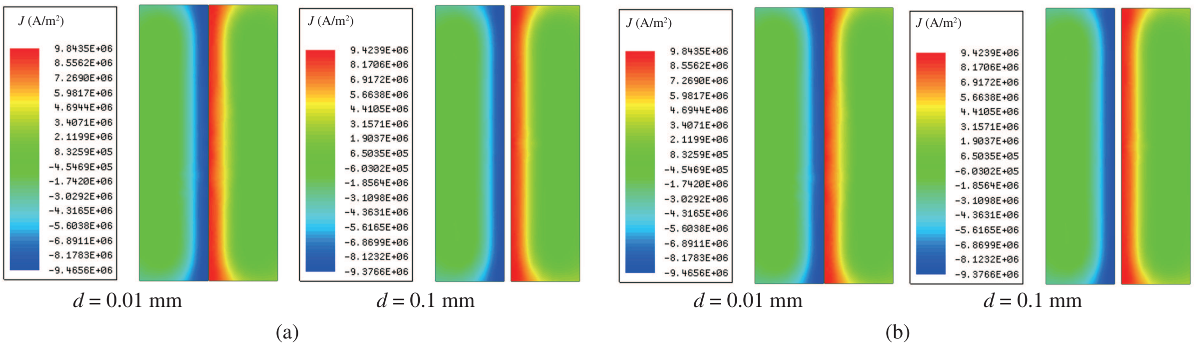

Figure 4 (Color online) Current density distribution. (a) Same current direction; (b) opposite current direction.

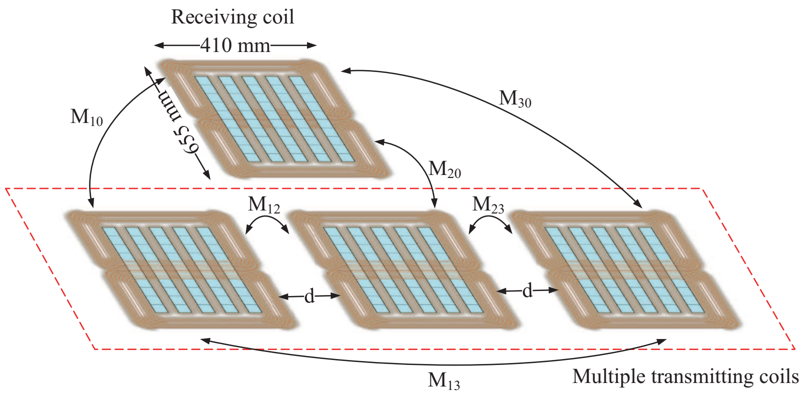

Figure 5 (Color online) Schematic diagram of multiple transmitting coils.

2.3 Loss model of the rectifier

The rectifier consists of four fast-recovery diodes, and indeed the conduction loss comes from the threshold voltage and on-resistance. Moreover, only two diodes are on at the same time, so we can get the rectifier loss as follows:

$$
\begin{aligned}
P_{\text{rec}} &= 2|I_{Lf0}|^2 r_{D1} + 2|I_{Lf0}|u_{D1} \\
&= \frac{2r_{D1}M^2|U_{AB}|^2}{\omega^2 L_{f1}^2 L_{f0}^2} + \frac{2u_{D1}M|U_{AB}|}{\omega L_{f1} L_{f0}}.
\end{aligned} \tag{7}
$$

3 Multiple transmitting networks

There are many issues to be considered in the design of the main coil. This paper does not discuss it in detail, but makes a simple explanation. At the same power level, the small size of the magnetically coupled main coil will bring a large power density, but it will also make it difficult to dissipate heat. In addition, the power of the wireless charging system is positively related to the mutual inductance between the energy transmitting coil and the receiving coil. The vertical distance between the receiving coil installed on the EV and the transmitting coil laid on the ground is about 200 mm. Therefore, the energy transmitting coil needs a large size to meet the mutual inductance requirement. Based on the above reasons, at the 10 kW power level, the structure and size of the magnetically coupled main coil in this paper are similar to [8]. In addition, Figure 5 is a schematic diagram of multiple transmitting coils under this structure. The transmitting and receiving coils are mirror-symmetrical when they are aligned.

3.1 Structure of multiple transmitting networks

Figure 6 illustrates the LCC-CCL resonance circuit of the multiple transmitting networks. The total mutual inductance of a coil j is $M_j = \sum_{i=0,i\neq j}^{n} M_{ij}$ with $M_{ij} = M_{ji}$ $(i \neq j)$ where the subscript 0 denotes the receiving coil and the subscripts 1–n represent the transmitting coils; M_{ij} is the mutual

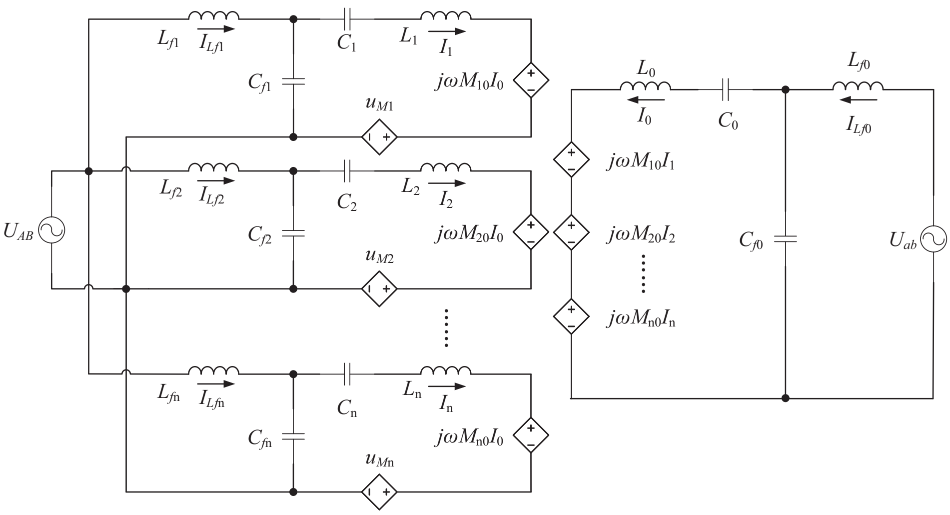

Figure 6 LCC-CCL resonance circuit of the multiple transmitting networks.

inductance between coils i and j; U_{AB}, U_{ab}, I_{Lfa}, and I_a are first-order signals where $a = 0, 1, \ldots, n$; $u_{Mi} = \sum_{b=1,b\neq i}^{n} j\omega M_{ib} I_b$, $i = 1, \ldots, n$. According to the analysis in [30], the resonance requires the parameters in the LCC-CCL to satisfy

$$C_{fa} = \frac{1}{\omega^2 L_{fa}}, \tag{8}$$

$$C_0 = \frac{1}{\omega^2 (L_0 - L_{f0})}, \tag{9}$$

$$\begin{bmatrix} X_1 C_{f1} \\ X_2 C_{f2} \\ \vdots \\ X_n C_{fn} \end{bmatrix} = - \begin{bmatrix} 0 & M_{12} & \cdots & M_{1n} \\ M_{21} & 0 & \cdots & M_{2n} \\ \vdots & \vdots & \ddots & \vdots \\ M_{n1} & M_{n2} & \cdots & 0 \end{bmatrix} \begin{bmatrix} C_{f1} \\ C_{f2} \\ \vdots \\ C_{fn} \end{bmatrix}, \tag{10}$$

where $X_i = L_i - \frac{1}{\omega^2 C_i} - \frac{1}{\omega^2 C_{fi}}$; ω is the resonant angular frequency. Indeed, through the resonance relationship of the circuit, we can obtain the LCC-CCL current expressions of the short-individual type DWC system as follows:

$$\begin{cases} |I_{Lfi}| = \dfrac{M_{i0}\,|U_{ab}|}{\omega L_{fi} L_{f0}}, \\ |I_i| = \dfrac{|U_{AB}|}{\omega L_{fi}}, \\ |I_0| = \dfrac{|U_{ab}|}{\omega L_{f0}}, \\ |I_{Lf0}| = \dfrac{|U_{AB}| \sum_{i=1}^{n} \frac{M_{i0}}{L_{fi}}}{\omega L_{f0}}, \end{cases} \tag{11}$$

where $|U_{AB}|$, $|U_{ab}|$, $|I_{Lfa}|$, and $|I_a|$ are rms values of U_{AB}, U_{ab}, I_{Lfa}, and I_a, respectively. Moreover, we keep the parameters of the transmitting network consistent, i.e., $L_{f1} = L_{f2} = \cdots = L_{fn}$; $L_1 = L_2 = \cdots = L_n$. Then we can get the following formula:

$$\begin{cases} |I_{Lfi}| = \dfrac{M_{i0}\,|U_{ab}|}{\omega L_{f1} L_{f0}}, \\ |I_i| = \dfrac{|U_{AB}|}{\omega L_{f1}}, \\ |I_0| = \dfrac{|U_{ab}|}{\omega L_{f0}}, \\ |I_{Lf0}| = \dfrac{M_0 |U_{AB}|}{\omega L_{f1} L_{f0}}, \end{cases} \tag{12}$$

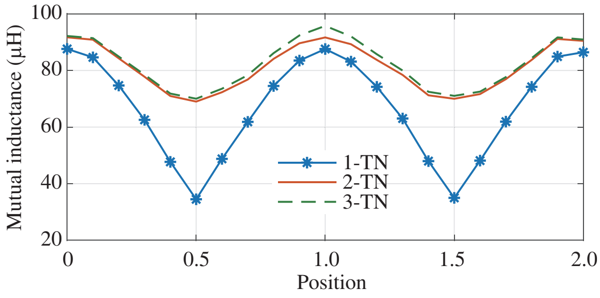

(a)

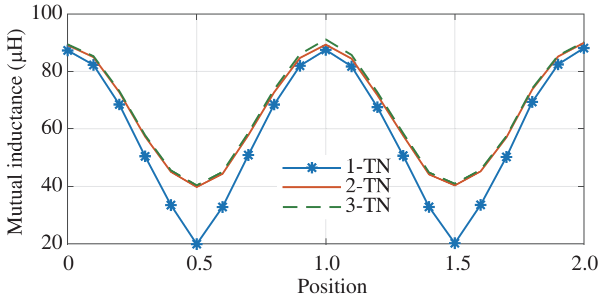

(b)

Figure 7 (Color online) Mutual inductance M_0 variations. (a) $x_{\rm s}=0.4$. (b) $x_{\rm s}=0.8$.

Table 3 Average mutual inductance under different i-TN and spacing

Spacing ($x_{\rm s}$)	1-TN (μH)	2-TN (μH)	3-TN (μH)
0	74.20	103.37	107.06
0.2	70.83	91.29	93.36
0.4	67.00	81.23	82.55
0.6	63.06	72.97	73.91
0.8	59.05	66.06	66.76
1	55.11	60.18	60.73

where $M_0=\sum_{i=1}^{n}M_{i0}$.

3.2 Analysis of number and spacing of multiple transmitting networks

We define the transmitting coil spacing as d and

$$d=x_{\rm s}c_{\rm L}, \tag{13}$$

where $x_{\rm s}\in[0,1]$ is the spacing proportion coefficient and $c_{\rm L}$ is the length of the transmitting coil in the direction of movement. Moreover, based on the model in Figure 5, we build the corresponding model in ANSYS. Under different spacing proportion coefficients $x_{\rm s}$, we can obtain the mutual inductance M_{i0} of the transmitting coil i to the receiving coil at different positions. Then, we can derive the sum of M_{i0} as M_0, i.e., $M_0=\sum_{i=1}^{n}M_{i0}$. In a set of transmitting equipment, we utilize i-TN to denote i transmitting networks in parallel, and accordingly, Figure 7 shows the results of the mutual inductance M_0 under 1-TN, 2-TN, and 3-TN. Positions 0–2 represent the alignments of the receiving coil with the transmitting coils 1–3, respectively.

In this part, we first consider the influence of the number of transmitting networks on mutual inductance M_0 in a set of transmitting equipment. Accordingly, we discuss three scenarios: 1-TN, 2-TN, and 3-TN. Indeed, the greater the number of transmitting networks in parallel is, the greater the total mutual inductance is. Here, the total mutual inductance refers to M_0. As shown in Figure 7, when the transmitting equipment has only one transmitting network, the mutual inductance M_0 fluctuates greatly. When two or three transmitting networks are in parallel, the fluctuation of mutual inductance M_0 is small. Moreover, to intuitively present the influence of different i-TN and spacing on mutual inductance M_0, we calculate the average value of M_0 at different positions when the i-TN and spacing are fixed. The results are shown in Table 3. It can be noticed that 2-TN and 3-TN have similar effects. When there are more than a certain number of transmitting networks in parallel, the transmitting coil far from the receiving coil has almost zero mutual inductance to the receiving coil. Therefore, a large number of transmitting networks connected in parallel can no longer improve the total mutual inductance M_0, and on the contrary, it will bring about a reduction in the efficiency of the DWC system. Accordingly, considering the power and efficiency comprehensively, this paper adopts the parallel operation mode of two transmitting networks. Then, we analyze the influence of spacing on mutual inductance M_0. As shown in Table 3, the smaller the spacing is, the greater the average value of mutual inductance M_0 is. Indeed, a small spacing will bring a large mutual inductance and form a high power, but it will also bring an increase in the cost of the short-individual type DWC system when the charging track length is constant. Accordingly, we can carry out multi-objective optimization between output power, efficiency, and cost by the transmitting coil spacing.

4 Multi-objective optimization strategy

4.1 Multi-objective optimization model

In the short-individual type DWC system, the loss models $P_{\rm hfi}$ and $P_{\rm rec}$ need to replace M in (2) and (7) with M_0 as follows:

$$P_{\rm hfi} = (1+r_{\rm p})\frac{2r_{S1}M_0^2|U_{ab}|^2}{\omega^2 L_{f1}^2 L_{f0}^2}, \tag{14}$$

$$P_{\rm rec} = \frac{2r_{D1}M_0^2|U_{AB}|^2}{\omega^2 L_{f1}^2 L_{f0}^2} + \frac{2u_{D1}M_0|U_{AB}|}{\omega L_{f1}L_{f0}}. \tag{15}$$

In addition, the loss model of the LCC-CCL resonance network should be adjusted as follows:

$$P_{a,{\rm LCC}}= |I_{Lfa}|^2 r_{Lfa} + |I_a|^2 r_a + (|I_{Lfa}|^2 + |I_a|^2) r_{Cfa}, \tag{16}$$

where $a = 0, 1, 2$. Since U_{ab} is a passive voltage generated by the rectifier, U_{ab} and I_{Lf0} have the same phase. Therefore, the output power of the LCC-CCL resonance network is

$$P_{ab} = |U_{ab}||I_{Lf0}| = \frac{M_0|U_{AB}||U_{ab}|}{\omega L_{f1}L_{f0}}. \tag{17}$$

Indeed, according to the energy conservation law, we have

$$P_{ab} = P_{\rm rec} + P_{\rm out}. \tag{18}$$

4.1.1 *Output power function*

Based on (18), we can get the output power:

$$P_{\rm out} = P_{ab} - P_{\rm rec}. \tag{19}$$

Accordingly, the average output power of a dynamic process is defined as follows:

$$P_{\rm aout} = \frac{1}{T}\int_0^T P_{\rm out}(t){\rm d}t, \tag{20}$$

where T denotes the time that the dynamic process consumes.

4.1.2 *Efficiency function*

According to (14)–(16), and (19), the system input power is

$$P_{\rm in} = P_{\rm out} + P_{\rm hfi} + \sum_{a=0}^{2} P_{a,{\rm LCC}} + P_{\rm rec}. \tag{21}$$

Similarly, we define the average input power as

$$P_{\rm ain} = \frac{1}{T}\int_0^T P_{\rm in}(t){\rm d}t. \tag{22}$$

Therefore, the efficiency of DWC system is

$$\eta = \frac{\int_0^T P_{\rm out}(t){\rm d}t}{\int_0^T P_{\rm in}(t){\rm d}t}. \tag{23}$$

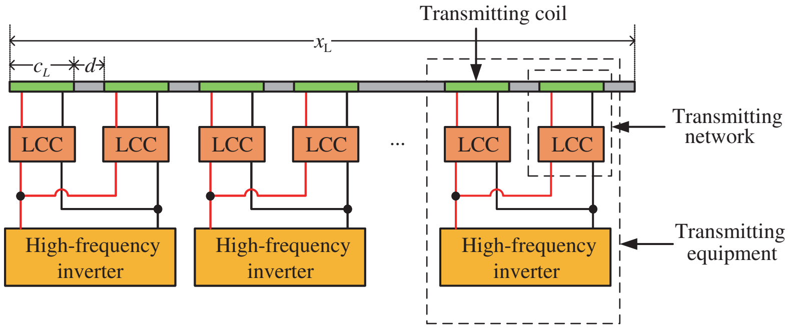

Figure 8 (Color online) Schematic diagram of charging track.

4.1.3 *Cost function*

As presented in Figure 8, we define the length of the charging track as $x_{\rm L}$. This paper utilizes two transmitting networks in parallel, so the number of transmitting equipment can be obtained as $N_t = \frac{x_{\rm L}}{2(c_{\rm L}+d)}$. The cost of each set of transmitting equipment is α, and the cost function is

$$\beta = \alpha \frac{x_{\rm L}}{2(c_{\rm L}+d)}. \tag{24}$$

Combining (13) and (24), we can obtain the cost function of $x_{\rm s}$ as

$$\beta = \alpha \frac{x_{\rm L}}{2c_{\rm L}(1+x_{\rm s})}. \tag{25}$$

Accordingly, we combine the output power, efficiency, and cost of the DWC system to form a multi-objective optimization problem as follows:

$$\begin{aligned} &\min_{x_{\rm s}} J(x_{\rm s}) = -(w_P \tilde{P}_{\rm aout}(x_{\rm s}) + w_\eta \tilde{\eta}(x_{\rm s})) + w_\beta \tilde{\beta}(x_{\rm s}),\\ &\text{s.t.} \quad 0 \leqslant x_{\rm s} \leqslant 1. \end{aligned} \tag{26}$$

Eq. (26) transforms the multi-objective optimization problem into the single-objective optimization problem. Indeed, the scale of each objective, i.e., the value range, is different. Then, it is difficult to find reasonable weight coefficients to unify the multi-objective problem. To solve this problem, we adopt a normalization form. The value range of each objective is normalized to [0, 1]. In this way, each objective has a unified scale, and the weight coefficients can be allocated as follows:

$$w_P + w_\eta + w_\beta = 1,$$

where $w_P \in [0,1]$, $w_\eta \in [0,1]$, and $w_\beta \in [0,1]$ are weight coefficients of $\tilde{P}_{\rm aout}$, $\tilde{\eta}$, and $\tilde{\beta}$, respectively. Correspondingly, $\tilde{P}_{\rm aout}$, $\tilde{\eta}$, and $\tilde{\beta}$ are normalized forms of $P_{\rm aout}$, η, and β, respectively. Indeed, the spacing affects the mutual inductance M_{i0}, which further affects $\tilde{P}_{\rm aout}$ and $\tilde{\eta}$. Therefore, both $\tilde{P}_{\rm aout}$ and $\tilde{\eta}$ can be expressed as a function of $x_{\rm s}$. The corresponding functional relationships can be obtained by data fitting. The fitting process and results are presented in Subsection 5.2.

4.2 Constrained adaptive particle swarm optimization

The optimization problem (26) is complex and difficult to be solved by analytic method. Therefore, we consider looking for other methods to solve the problem. The particle swarm optimization (PSO) [34–36] belongs to a heuristic learning method, which is suitable for dealing with complex problems. The main parameters of PSO are population size $N_{\rm s}$, spatial search dimension N_D, iteration number N_M, inertia weight w, self-learning factor s_1, swarm learning factor s_2, velocity V, and position X. However, the PSO with fixed inertia weight, self-learning factor, and swarm learning factor is difficult to balance global search and local search. Meanwhile, there are no constraints on decision variables. Therefore, we propose an improved PSO algorithm. The improved algorithm adds constraints on decision variables. In addition,

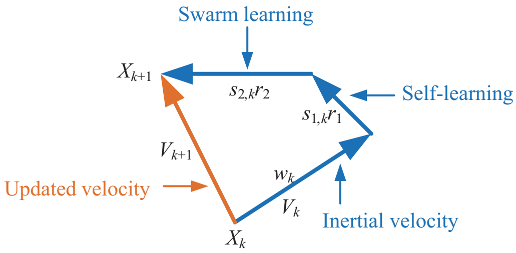

Figure 9 (Color online) Schematic diagram of particle velocity and position update.

to balance the global search capability and local improvement capability of the PSO algorithm, we adopt the method of adaptive inertia weight as follows:

$$w_k = \begin{cases} w_l + \frac{(f_{x,k}-f_{\min,k})(w_u-w_l)}{f_{\text{ave},k}-f_{\min,k}}, & f_{x,k} \leqslant f_{\text{ave},k}, \\ w_u, & f_{x,k} > f_{\text{ave},k}, \end{cases} \tag{27}$$

where w_u and w_l are the upper and lower bounds of w_k; $f_{x,k}$ is the functional value of the particle at step k; $f_{\min,k}$ and $f_{\text{ave},k}$ are the minimum and average values of the swarm at step k. When the objective function value $f_{x,k}$ is lower than the average value $f_{\text{ave},k}$, the inertia weight is small, the movement range of particle is weakened, and the local search capability is strong. When the objective function value $f_{x,k}$ is higher than the average value $f_{\text{ave},k}$, the inertia weight is large, which makes the particle move closer to the better region. The global search capability is strong. Meanwhile, we adopt learning factors of asynchronous change. In the initial stage of optimization, particles have a large self-learning factor and a small swarm learning factor, which is beneficial to strengthen the global search capability. In the later stage of optimization, particles have a small self-learning factor and a large swarm learning factor, which is conducive to convergence to the global optimal solution. The expressions of the asynchronous change learning factors are as follows:

$$s_{1,k} = s_{1,\text{ini}} + \frac{s_{1,\text{fin}} - s_{1,\text{ini}}}{N_M}k, \tag{28}$$

$$s_{2,k} = s_{2,\text{ini}} + \frac{s_{1,\text{fin}} - s_{1,\text{ini}}}{N_M}k, \tag{29}$$

where $s_{1,k}$ is the self-learning factor at step k; $s_{2,k}$ is the swarm learning factor at step k; $s_{1,\text{ini}}$ and $s_{2,\text{ini}}$ represent the initial values of s_1 and s_2, respectively; $s_{1,\text{fin}}$ and $s_{2,\text{fin}}$ represent the final values of s_1 and s_2, respectively; k represents the current iteration step.

Since w_k, $s_{1,k}$, and $s_{2,k}$ all change with the iteration step k, it is called an adaptive algorithm. In addition, due to the existence of constraints on decision variables, the improved PSO proposed in this paper is called the CAPSO algorithm. This algorithm has the advantages of being able to constrain decision variables and being easy to handle complex optimization problems, as well as it has high accuracy. Therefore, the CAPSO algorithm is proposed in this paper to solve the optimization problem. In addition, Figure 9 presents the schematic diagram of particle velocity and position update. The updated velocity is determined by three parts: inertial velocity, self-learning, and swarm learning. The update expressions for velocity and position are

$$V_{k+1} = w_k V_k + s_{1,k} r_1 (X_{\text{p}} - X_k) + s_{2,k} r_2 (X_o - X_k), \tag{30}$$

$$X_{k+1} = X_k + V_{k+1}, \tag{31}$$

where r_1 and r_2 are random numbers between 0 and 1; X_{p} is the historical optimal position of the particle; X_o is the historical optimal position of the swarm. Accordingly, we are able to obtain the CAPSO algorithm presented in Figure 10.

5 Simulation results

5.1 Feasibility verification

According to [37], Table 4 lists the system parameters. First, we build a wireless charging system in PLECS to obtain the simulation results. Then, we build mathematical models of loss in MATLAB to

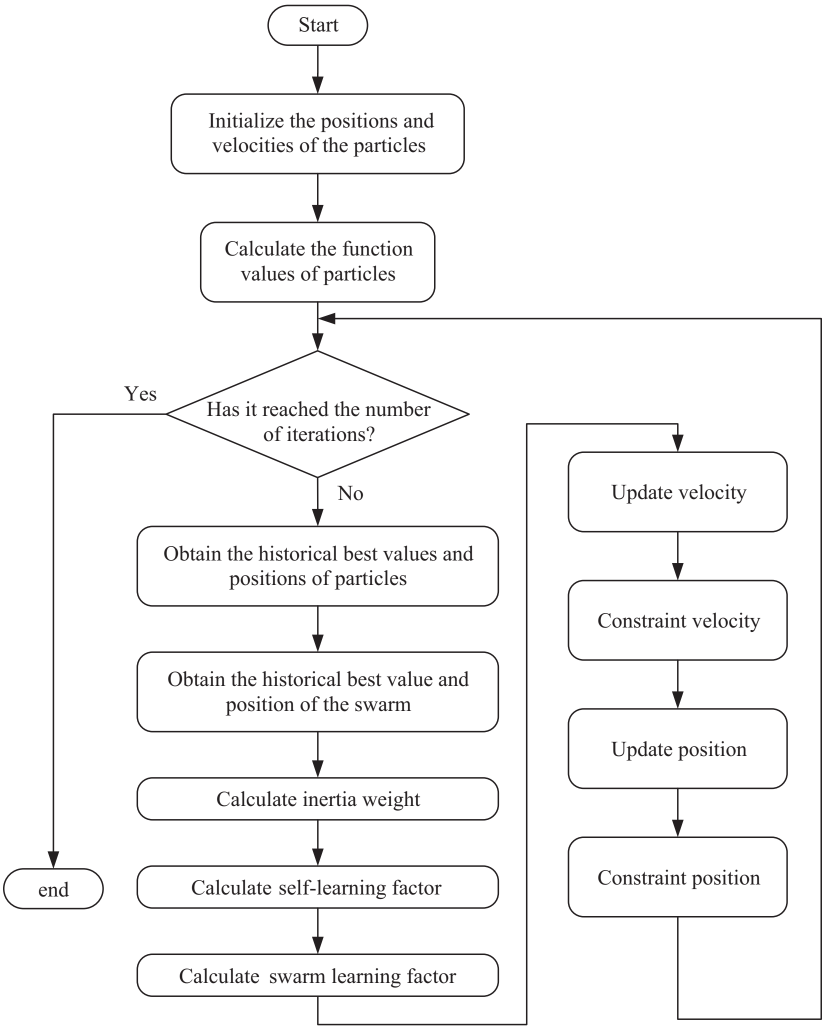

Figure 10 CAPSO algorithm flow chart.

Table 4 System parameters

Symbol	Value	Symbol	Value	Symbol	Value
u_{in}	500 V	u_B	330 V	r_{Cf1}	10 mΩ
L_1	420 μH	M	70 μH	r_{Cf0}	10 mΩ
L_0	420 μH	C	165 μF	r_{D1}	6.1 mΩ
L_{f1}	45 μH	L	3 mH	u_{D1}	1.43 V
L_{f0}	45 μH	r_{S1}	30 mΩ	r_{S5}	30 mΩ
C_{f1}	77.91 nF	r_{Lf1}	30 mΩ	u_{S5}	0.85 V
C_{f0}	77.91 nF	r_{Lf0}	30 mΩ	r_{D5}	4.4 mΩ
C_1	9.35 nF·Ω	r_1	300 mΩ	u_{D5}	1.1 V
C_0	9.65 nF·Ω	r_0	300 mΩ	r_{L}	300 mΩ

obtain the calculation results. The simulation and calculation results of the loss model are presented in Table 5. We define the simulation results and calculation results by y_{s} and y_{c}, respectively. The average value of the relative error is described as follows:

$$\varepsilon = \frac{1}{4}\sum_{i=1}^{4}\frac{|y_{\mathrm{s},i} - y_{\mathrm{c},i}|}{y_{\mathrm{s},i}} \times 100\%,$$

where $i = 1$, 2, 3, and 4 represent the cases of P_{hfi}, P_{LCC}, P_{rec}, and P_{out}, respectively. Based on the data in Table 5, we have $\varepsilon = 1.73\%$, which indicates that the simulation and calculation results tend to be consistent. Therefore, we are able to consider the approximation of (1) to be reasonable.

Table 5 Loss comparison results of simulation and calculation

	Simulation results (W)	Calculation results (W)
$P_{\rm hfi}$	24.65	23.18
$P_{\rm LCC}$	205.10	204.89
$P_{\rm rec}$	92.97	93.69
$P_{\rm out}$	8569.04	8562.93

Table 6 Polynomial coefficients

Coefficient	Average output power	Efficiency
a_0	9587	0.9532
a_1	−6661	−0.01251
a_2	3399	−0.005323
a_3	−902.1	0.001489

5.2 Data fitting process and results

In (25), the cost is a function of $x_{\rm s}$. However, for the average output power $P_{\rm aout}$ and efficiency η of the DWC system, due to the complexity of expressions, it is necessary to carry out data fitting to obtain functional relationships with respect to $x_{\rm s}$. According to (12), (14)–(19) and (21), it can be concluded that the output power $P_{\rm out}$ and input power $P_{\rm in}$ are functions of M_{i0}. Subsequently, we can obtain the mutual inductance M_{i0} in ANSYS, which is a function of position p. Here, $p \in [0, 2]$. $p = 0$, 1, and 2 represent the alignments of the receiving coil with the transmitting coils 1, 2, and 3, respectively. Then, both the output power $P_{\rm out}$ and input power $P_{\rm in}$ can be expressed as functions of p. In the case of a fixed spacing proportion coefficient $x_{\rm s}$, we calculate the average output power $P_{\rm aout}$ and efficiency η of the DWC system through (20) and (23). Moreover, we need to convert the integral operations in (20) and (23) into the sum operations because the data are discrete. The calculation method is as follows:

$$P_{\rm aout} = \frac{1}{N_{\rm p}} \sum_{i=1}^{N_{\rm p}} P_{\rm out}(p_i), \tag{32}$$

$$\eta = \frac{\sum_{i=1}^{N_{\rm p}} P_{\rm out}(p_i)}{\sum_{i=1}^{N_{\rm p}} P_{\rm in}(p_i)}, \tag{33}$$

where $N_{\rm p}$ is the number of discrete data. p_i is a discrete position variable. Indeed, under each $x_{\rm s}$, we can derive a corresponding $P_{\rm aout}$ and a corresponding η, and then $P_{\rm aout}$ and η can be expressed as a function of $x_{\rm s}$. Now, we need to fit the expressions through the data points $(x_{\rm s}, P_{\rm aout})$ and $(x_{\rm s}, \eta)$. We can complete the fitting through the curve fitting tool. In the least squares fitting of discrete data, the simplest and most practical mathematical model is a polynomial. Meanwhile, to ensure the fitting accuracy and avoid overfitting, we choose the polynomial order as 3. The expression is as follows:

$$f(x_{\rm s}) = a_0 + a_1 x_{\rm s} + a_2 x_{\rm s}^2 + a_3 x_{\rm s}^3, \tag{34}$$

where a_i is the polynomial coefficient and their values are shown in Table 6. Figure 11 presents the fitting results, which illustrates that the polynomial fitting has a good effect.

5.3 Algorithm comparison

Ref. [38] gave a constrained adaptive weight PSO (CWPSO) algorithm where the inertia weight changes with the change of the iteration step. Our contribution to the optimization method is to propose the asynchronously changing self-learning factor and swarm learning factor in addition to introducing adaptive inertia weight. Subsequently, we compare the basic constrained PSO (CPSO), CWPSO, and CAPSO proposed in this paper. The parameters of CPSO, CWPSO, and CAPSO are shown in Table 7.

We use the following benchmark optimization problem for the algorithm performance test, which is given by

$$\begin{aligned} &\min_{x,y} f(x,y) = 20 + x^2 - 10\cos(2\pi x) + y^2 - 10\cos(2\pi y) \\ &\text{s.t.} \quad -5 \leqslant x \leqslant 5, \\ &\qquad\ \ -5 \leqslant y \leqslant 5. \end{aligned} \tag{35}$$

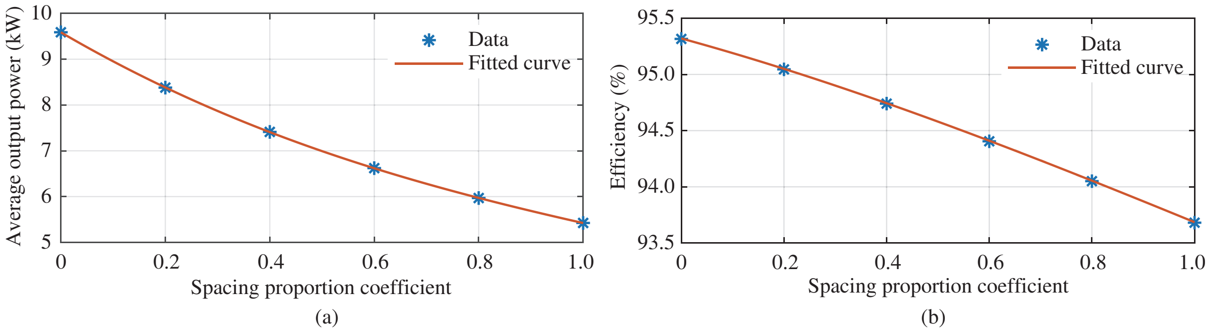

Figure 11 (Color online) Fitting results. (a) Average output power; (b) efficiency.

Table 7 Parameters of the three algorithms

Parameter	Symbol	CPSO	CWPSO	CAPSO
Population size	$N_{\rm s}$	1000	1000	1000
Iteration number	N_M	100	100	100
Inertia weight	w	0.7	–	–
Self-learning factor	s_1	2.5	2.5	–
Swarm learning factor	s_2	2.5	2.5	–
Upper bound of inertia weight	w_u	–	0.8	0.8
Lower bound of inertia weight	w_l	–	0.6	0.6
Initial value of self-learning factor	$s_{1,\rm ini}$	–	–	2.5
Final value of self-learning factor	$s_{1,\rm fin}$	–	–	0.5
Initial value of swarm learning factor	$s_{2,\rm ini}$	–	–	0.5
Final value of swarm learning factor	$s_{2,\rm fin}$	–	–	2.5

Table 8 Results under different algorithms

Decision variable	CPSO	CWPSO	CAPSO
x	−6.28E−06	9.66E−07	5.05E−11
y	7.82E−06	5.24E−07	−6.25E−11

The optimization problem (35) has a unique global optimal solution $(0, 0)$. Then, we utilize CPSO, CWPSO, and CAPSO to solve (35), respectively. Under each algorithm, we perform 100 calculations. The final results are averaged and presented in Table 8. In the later stage of iteration, the CAPSO algorithm has a small self-learning factor and a large swarm learning factor, which can well converge to the global optimal solution. Accordingly, compared with CPSO and CWPSO, the proposed CAPSO algorithm has higher accuracy. The disadvantage of the proposed CAPSO algorithm is that the inertia weight, self-learning factor, and swarm learning factor need to be calculated in each iteration, which will cause a small increase in the amount of calculation.

5.4 Optimization results

We take the DWC system with a 10 km long road and 10 kW rated power to discuss the optimization results under different weight coefficients. Considering the cost in [8], we take the cost coefficient α as 1000. According to the analysis in Subsection 5.3, the CAPSO algorithm proposed in this paper has high accuracy, so it is used to solve the multi-objective optimization problem (26).

Table 9 shows the optimization results of the proposed CAPSO algorithm under different weight combinations. The parameters of the CAPSO algorithm are shown in Table 7. Moreover, Figure 12 illustrates the convergence curves of the CAPSO algorithm under two different weight combinations. Under the weight combination 1, $w_P = 0.25$, $w_\eta = 0.25$, and $w_\beta = 0.5$; under the weight combination 2, $w_P = 0.2$, $w_\eta = 0.2$, and $w_\beta = 0.6$. The results show that the CAPSO algorithm achieves a stable state within 30 steps and has good convergence performance. Under different weight combinations, a series of optimal spacing proportion coefficients $x_{\rm s}$ can be solved. Accordingly, the average output power $P_{\rm aout}$, efficiency η, and cost β can be calculated from $x_{\rm s}$. As presented in Figure 11, both $P_{\rm aout}$ and η decrease with the increase of $x_{\rm s}$. Accordingly, in the multi-objective optimization problem, $-\tilde{P}_{\rm aout}$ and $-\tilde{\eta}$ have a

Table 9 Optimization results under different weight combinations

w_P	w_η	w_β	x_s	P_{aout} (kW)	η (%)	β (dollars in millions)
1	0	0	0	9.5870	95.32	12.1951
0.6	0.2	0.2	0	9.5870	95.32	12.1951
0.33	0.33	0.34	0	9.5870	95.32	12.1951
0.3	0.3	0.4	0.0792	9.0805	95.22	11.3004
0.45	0.1	0.45	0.1165	8.8557	95.17	10.9226
0.35	0.2	0.45	0.1902	8.4366	95.06	10.2459
0.25	0.25	0.5	0.4036	7.3931	94.74	8.6886
0.2	0.25	0.55	0.5877	6.6634	94.43	7.6812
0.35	0.1	0.55	0.7023	6.2728	94.23	7.1638
0.2	0.2	0.6	0.8186	5.9173	94.02	6.7059
0.15	0.15	0.7	1	5.4229	93.69	6.0976
0	0	1	1	5.4229	93.69	6.0976

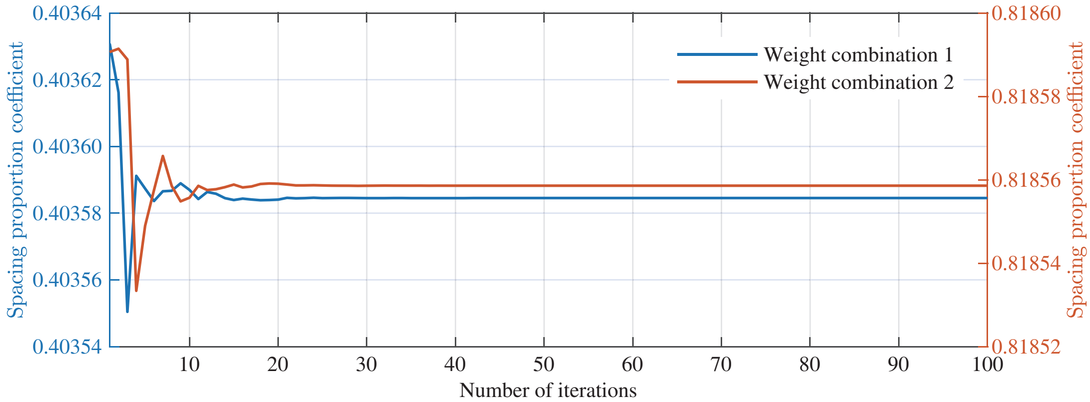

Figure 12 (Color online) Convergence curves of CAPSO algorithm.

positive correlation with x_s, and $\tilde{\beta}$ has a negative correlation with x_s. As shown in Table 9, x_s is greater than 0 only when $w_P + w_\eta$ is less than or equal to 0.6. Here, $w_P + w_\eta$ indicates the weight sum of the positive correlation functions with x_s. Then, w_β indicates the weight of the negative correlation function with x_s. When the positive correlation part has the same proportion as the negative correlation part in the multi-objective optimization, i.e., $w_P + w_\eta = w_\beta$, we have $x_s = 0.4036$, $P_{aout} = 7.3931$ kW, $\eta = 94.74\%$, and $\beta = 8.6886$ dollars in millions where $w_P = w_\eta$; when the the positive correlation part accounts for a large proportion, such as $w_P = 0.6$, $w_\eta = 0.2$, and $w_\beta = 0.2$, we have $x_s = 0$, $P_{aout} = 9.587$ kW, $\eta = 95.32\%$, and $\beta = 12.1951$ dollars in millions; when the the negative correlation part accounts for a large proportion, such as $w_P = 0.15$, $w_\eta = 0.15$, and $w_\beta = 0.7$, we have $x_s = 1$, $P_{aout} = 5.4229$ kW, $\eta = 93.69\%$, and $\beta = 6.0976$ dollars in millions. Indeed, the allocation of weight coefficients will affect optimal function values. No matter how the weight coefficients are allocated, each objective cannot reach the optimal value at the same time. Therefore, we need to set the weight coefficient reasonably according to the emphasis of three objectives in different scenarios.

6 Conclusion

This paper presents a multi-objective optimization method for the output power, efficiency, and cost of the short-individual type DWC system. We first analyze the loss model of the static wireless system in detail, and then extend the static wireless charging to the DWC and obtain the corresponding DWC loss model. Then, by establishing the function of output power, efficiency, and cost with respect to x_s, we construct a multi-objective optimization problem. Moreover, the expressions of output power and efficiency are derived through data fitting. In Section 5, we first verify the feasibility and rationality of the proposed model, and then present the data fitting process and results. Subsequently, we compare the proposed CAPSO with CPSO and CWPSO. The results show that the CAPSO algorithm is more accurate, so it is used for multi-objective optimization. Finally, we take the DWC system with a length of 10 km and rated power of 10 kW as an example to show the optimization results under different weight combinations. We can adopt a trade-off between the physical and economic indexes, and allocate appropriate weights to the objectives, so that the corresponding optimization results can be obtained.

Acknowledgements This work was partially supported by National Key R&D Program of China (Grant No. 2018YFA0703800), Science Fund for Creative Research Group of the National Natural Science Foundation of China (Grant No. 61621002), and Zhejiang Key R&D Program (Grant No. 2021C01198).

References

1 Budhia M, Covic G A, Boys J T. Design and optimization of circular magnetic structures for lumped inductive power transfer systems. IEEE Trans Power Electron, 2011, 26: 3096–3108

2 Budhia M, Boys J T, Covic G A, et al. Development of a single-sided flux magnetic coupler for electric vehicle IPT charging systems. IEEE Trans Ind Electron, 2013, 60: 318–328

3 Zaheer A, Hao H, Covic G A, et al. Investigation of multiple decoupled coil primary pad topologies in lumped IPT systems for interoperable electric vehicle charging. IEEE Trans Power Electron, 2015, 30: 1937–1955

4 Wang C S, Covic G A, Stielau O H. Power transfer capability and bifurcation phenomena of loosely coupled inductive power transfer systems. IEEE Trans Ind Electron, 2004, 51: 148–157

5 Li S, Li W, Deng J, et al. A double-sided LCC compensation network and its tuning method for wireless power transfer. IEEE Trans Veh Technol, 2015, 64: 2261–2273

6 Li W, Zhao H, Li S, et al. Integrated LCC compensation topology for wireless charger in electric and plug-in electric vehicles. IEEE Trans Ind Electron, 2015, 62: 4215–4225

7 Deng J, Li W, Nguyen T D, et al. Compact and efficient bipolar coupler for wireless power chargers: design and analysis. IEEE Trans Power Electron, 2015, 30: 6130–6140

8 Zhou Z, Zhang L, Liu Z, et al. Model predictive control for the receiving-side DC-DC converter of dynamic wireless power transfer. IEEE Trans Power Electron, 2020, 35: 8985–8997

9 Miller J M, Onar O C, Chinthavali M. Primary-side power flow control of wireless power transfer for electric vehicle charging. IEEE J Emerg Sel Top Power Electron, 2015, 3: 147–162

10 Chen F, Garnier H, Deng Q, et al. Control-oriented modeling of wireless power transfer systems with phase-shift control. IEEE Trans Power Electron, 2020, 35: 2119–2134

11 Kato M, Imura T, Hori Y. Study on maximize efficiency by secondary side control using DC-DC converter in wireless power transfer via magnetic resonant coupling. In: Proceedings of World Electric Vehicle Symposium and Exhibition (EVS27), Barcelona, 2013. 1–5

12 Zhou Z, Zhang L Y, Liu Z T, et al. Design and demonstration of a dynamic wireless power transfer system for electric vehicles. Sci China Inf Sci, 2019, 62: 224201

13 Dai X, Li X, Li Y, et al. Maximum efficiency tracking for wireless power transfer systems with dynamic coupling coefficient estimation. IEEE Trans Power Electron, 2018, 33: 5005–5015

14 Miller J M, Jones P T, Li J M, et al. ORNL experience and challenges facing dynamic wireless power charging of EV's. IEEE Circ Syst Mag, 2015, 15: 40–53

15 Ko Y D, Jang Y J. The optimal system design of the online electric vehicle utilizing wireless power transmission technology. IEEE Trans Intell Transp Syst, 2013, 14: 1255–1265

16 Tavakoli R, Pantic Z. Analysis, design, and demonstration of a 25-kW dynamic wireless charging system for roadway electric vehicles. IEEE J Emerg Sel Top Power Electron, 2018, 6: 1378–1393

17 Li S, Wang L, Guo Y, et al. Power stabilization with double transmitting coils and T-type compensation network for dynamic wireless charging of EV. IEEE J Emerg Sel Top Power Electron, 2020, 8: 1801–1812

18 Vu V B, Dahidah M, Pickert V, et al. A high-power multiphase wireless dynamic charging system with low output power pulsation for electric vehicles. IEEE J Emerg Sel Top Power Electron, 2020, 8: 3592–3608

19 Wei W, Mei S, Wu L, et al. Optimal traffic-power flow in urban electrified transportation networks. IEEE Trans Smart Grid, 2017, 8: 84–95

20 Manshadi S D, Khodayar M E, Abdelghany K, et al. Wireless charging of electric vehicles in electricity and transportation networks. IEEE Trans Smart Grid, 2018, 9: 4503–4512

21 Lv S, Wei Z, Sun G, et al. Optimal power and semi-dynamic traffic flow in urban electrified transportation networks. IEEE Trans Smart Grid, 2020, 11: 1854–1865

22 Dai X, Jiang J C, Wu J Q. Charging area determining and power enhancement method for multiexcitation unit configuration of wirelessly dynamic charging EV system. IEEE Trans Ind Electron, 2019, 66: 4086–4096

23 Zhao J, Luo C, Ma S, et al. Control method of magnetic resonant WPT maintaining stable transmission power with wide misalignment tolerance. J Eng, 2019, 2019: 3392–3395

24 Zhang X, Yuan Z, Yang Q, et al. Coil design and efficiency analysis for dynamic wireless charging system for electric vehicles. IEEE Trans Magn, 2016, 52: 1–4

25 Liu Y, Mai R, Liu D, et al. Efficiency optimization for wireless dynamic charging system with overlapped DD coil arrays. IEEE Trans Power Electron, 2018, 33: 2832–2846

26 Kim D H, Ahn D. Maximum efficiency point tracking for multiple-transmitter wireless power transfer. IEEE Trans Power Electron, 2020, 35: 11391–11400

27 Shin J, Shin S, Kim Y, et al. Design and implementation of shaped magnetic-resonance-based wireless power transfer system for roadway-powered moving electric vehicles. IEEE Trans Ind Electron, 2014, 61: 1179–1192

28 Prasanth V, Bauer P. Distributed IPT systems for dynamic powering: misalignment analysis. IEEE Trans Ind Electron, 2014, 61: 6013–6021

29 Miller J M, Onar O C, White C, et al. Demonstrating dynamic wireless charging of an electric vehicle: the benefit of electrochemical capacitor smoothing. IEEE Power Electron Mag, 2014, 1: 12–24

30 Lu F, Zhang H, Hofmann H, et al. A dynamic charging system with reduced output power pulsation for electric vehicles. IEEE Trans Ind Electron, 2016, 63: 6580–6590

31 Azad A N, Echols A, Kulyukin V A, et al. Analysis, optimization, and demonstration of a vehicular detection system intended for dynamic wireless charging applications. IEEE Trans Transp Electrific, 2019, 5: 147–161

32 Erickson R W, Maksimovic D. Fundamentals of Power Electronics. 2nd ed. New York: Academic, 2001

33 Sullivan C R, Zhang R Y. Analytical model for effects of twisting on litz-wire losses. In: Proceedings of IEEE 15th Workshop on Control and Modeling for Power Electronics (COMPEL), Santander, 2014. 1–10

34 Kennedy J, Eberhart R. Particle swarm optimization. In: Proceedings of International Conference on Neural Networks, Perth, 1995. 4: 1942–1948

35 Shi Y, Eberhart R. A modified particle swarm optimizer. In: Proceedings of IEEE International Conference on Evolutionary Computation Proceedings, Anchorage, 1998. 69–73

36 Clerc M, Kennedy J. The particle swarm-explosion, stability, and convergence in a multidimensional complex space. IEEE Trans Evol Computat, 2002, 6: 58–73

37 Zhou Z, Liu Z, Su H. Multi-objective optimization of the wireless power transfer system for electric vehicles. In: Proceedings of IEEE Wireless Power Transfer Conference (WPTC), Seoul, 2020. 215–218

38 Zheng Q, Liang Y-G. A study on the particle swarm optimization with adaptive weight constrained layout optimization. In: Proceedings of the 8th International Conference on Intelligent Human-Machine Systems and Cybernetics (IHMSC), Hangzhou, 2016. 283–287